

# Triaxial Haloes and Particle Dark Matter Detection

N.W. Evans<sup>1</sup>, C.M. Carollo<sup>2</sup> & P.T. de Zeeuw<sup>3</sup>

<sup>1</sup>*Theoretical Physics, Department of Physics, 1 Keble Road, Oxford, OX1 3NP*

<sup>2</sup>*Department of Astronomy, Columbia University, 538 W. 120th Street, New York, NY 10027, USA*

<sup>3</sup>*Sterrewacht Leiden, Postbus 9513, 2300 RA Leiden, The Netherlands*

## ABSTRACT

This paper presents the properties of a family of scale-free triaxial haloes. We adduce arguments to suggest that the velocity ellipsoids of such models are aligned in conical coordinates. We provide an algorithm to find the set of conically aligned velocity second moments that support a given density against the gravity field of the halo. The case of the logarithmic ellipsoidal model – *the simplest triaxial generalisation of the familiar isothermal sphere* – is examined in detail. The velocity dispersions required to hold up the self-consistent model are analytic. The velocity distribution of the dark matter can be approximated as a triaxial Gaussian with semiaxes equal to the velocity dispersions.

There are roughly twenty experiments worldwide that are searching for evidence of scarce interactions between weakly-interacting massive-particle dark matter (WIMPs) and detector nuclei. The annual modulation signal, caused by the Earth’s rotation around the Sun, is a crucial discriminant between WIMP events and the background. The greatest rate is in June, the least in December. We compute the differential detection rate for energy deposited by the rare WIMP-nucleus interactions in our logarithmic ellipsoidal halo models. Triaxiality and velocity anisotropy change the total rate by up to  $\sim 40\%$ , and have a substantial effect on the amplitude of the annual modulation signal. The overall rate is greatest, but the amplitude of the modulation is weakest, in our radially anisotropic halo models. Even the sign of the signal can be changed. Restricting attention to low energy events, the models predict that the maximum rate occurs in December, and not in June.

**Key words:** dark matter – galaxies: haloes – galaxies: kinematics and dynamics – galaxies: structure – celestial mechanics, stellar dynamics

## 1 INTRODUCTION

The construction of velocity distributions for triaxial haloes is a hard problem. Jeans’ theorem guarantees that the distribution function depends only on the isolating integrals of motion. Generally, motion in a triaxial potential admits only one exact integral of motion, the energy or the Jacobi constant for the case of figure rotation. As Schwarzschild (1981) has articulated, it seems that self-consistent triaxial equilibrium configurations can exist only if the potential has additionally two effective, non-classical integrals. To date, the most general and successful method for building triaxial models has been the numerical combination of orbit densities, often called Schwarzschild’s (1979, 1982) method. Recent applications and extensions of the method to triaxial modelling are given by Merritt & Fridman (1996), Zhao (1996) and Häfner et al. (2000).

Given the difficulty of the task, it is often the case that only the lowest order velocity moments of the distribution function are calculated via the Jeans equations (sometimes called the stellar hydrodynamical equations). This is because the moments are easier to obtain and are related directly to

observable properties. Many solutions of the Jeans equations have been derived for spherical and axisymmetric systems (e.g., Binney & Mamon 1982; Bacon 1985; Fillmore 1986; Amendt & Cuddeford 1991). Even though it is not always evident whether such solutions correspond to dynamical models with positive definite distribution functions, these studies have been useful. For example, starting configurations for  $N$ -body experiments can be generated by assuming that the velocity distributions are Gaussians with semi-axes as prescribed by the Jeans solutions. Of course, this is only an approximation, but it is an excellent one and in routine use (e.g., Barnes 1994).

The simplest model of all for a dark halo is the isothermal sphere. This is commonly used to estimate the rates in both microlensing and non-baryonic dark matter detection experiments (e.g., Paczyński 1986; Jungman, Kamionkowski & Griest 1996; Lewin & Smith 1996). There is no reason whatsoever why dark matter haloes should be spherical, and there is ample evidence from external galaxies that haloes are generically flattened (e.g., Sackett et al. 1994; Olling 1995, 1996). In this paper, we present a number of properties of one of the simplest triaxial halo models – the logarithmic

mic ellipsoidal potential (e.g., Binney & Tremaine 1987; de Zeeuw & Pfenniger 1988; Miralda-Escudé & Schwarzschild 1989). This is the natural triaxial generalisation of the singular isothermal sphere. Self-consistent distributions of velocities for this model are not known, but here we provide simple and analytic solutions of the Jeans equations. These solutions are aligned in conical coordinates and provide the velocity second moments required to support the triaxial dark halo against gravity.

One possibility is that galaxy haloes are composed of weakly-interacting massive-particle (WIMP) dark matter. Direct detection experiments measure the energy deposited by the rare interactions between the WIMP and the detector nucleus. There are now about 20 direct detection experiments running or in preparation worldwide (e.g., articles in Klapdor-Kleingrothaus & Ramachers 1997 and Spooner 1997). One of the main difficulties in the experiments is how to distinguish between the recoil events caused by WIMPs and those caused by radioactivity in the surroundings and by cosmic rays. One suggestion is that the annual modulation in the WIMP signal, caused by the motion of the Earth around the Sun, may be a powerful diagnostic (Freese, Frieman & Gould 1985). In fact, one of the experimental groups (DAMA) has very recently claimed detection of this modulation (Bernabei et al. 1999a,b), though the validity of this claim is still a matter of fierce debate (e.g., Gerbier et al. 1997, 1999; Abusaiadi et al. 2000). This paper investigates the dependence of this differential rate and the annual modulation on the triaxial shape and velocity distribution of the dark matter halo.

The paper is arranged as follows. Section 2 introduces the scale-free halo models under scrutiny, while Section 3 derives and solves the Jeans equations for the velocity second moments under the assumption of conical alignment. A number of reasons are given in support of our assumption as to the orientation of the velocity dispersion tensor. The properties of the logarithmic ellipsoidal halo models – the intrinsic and projected shapes and velocities – are found in Section 4. Finally, Section 5 considers the application to direct detection experiments in some detail.

## 2 TRIAXIAL HALO MODELS

One of the most widely-used axisymmetric halo models is the logarithmic scale-free potential investigated by Toomre in the 1970s (see Toomre 1982) and subsequently studied by others (e.g., Richstone 1980; Evans 1993). Its equipotential surfaces are spheroids. The analogous scale-free triaxial halo models have equipotentials that are triaxial ellipsoids with axis ratios  $p$  and  $q$  (e.g., Binney 1981; de Zeeuw & Pfenniger 1988). We shall call them *the logarithmic ellipsoidal models*. In Cartesian coordinates, the potential-density pair is given by:

$$\Phi(x, y, z) = \frac{1}{2}v_c^2 \ln(x^2 + y^2 p^{-2} + z^2 q^{-2}) \quad (2.1)$$

and

$$\rho(x, y, z) = \frac{v_c^2}{4\pi G} \frac{Ax^2 + By^2 p^{-2} + Cz^2 q^{-2}}{(x^2 + y^2 p^{-2} + z^2 q^{-2})^2}, \quad (2.2)$$

with

$$\begin{aligned} A &= p^{-2} + q^{-2} - 1, & B &= 1 + q^{-2} - p^{-2}, \\ C &= 1 + p^{-2} - q^{-2}. \end{aligned} \quad (2.3)$$

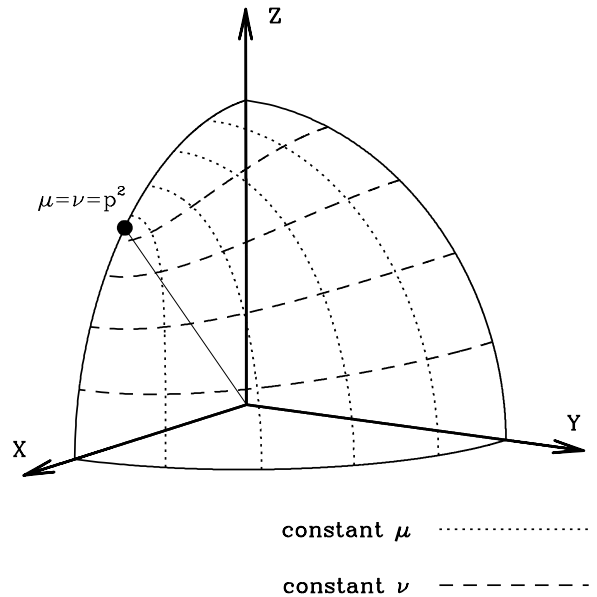


**Figure 1.** The coordinate curves  $(\mu, \nu)$  on the surface of the sphere. If the radius of the sphere is  $r$ , then the set  $(r, \mu, \nu)$  provides a triply-orthogonal set of coordinate surfaces. The filled dot indicates the point  $\mu = \nu = p^2$ ; it lies in the  $(x, z)$ -plane, at  $x = r\sqrt{T}$ ,  $z = r\sqrt{1-T}$ , with  $T = (1-p^2)/(1-q^2)$  the triaxiality parameter.

The rotation curve is completely flat with amplitude  $v_c$ . This potential therefore describes a triaxial halo with a flat rotation curve. Without loss of generality, we require  $q^2 \leq p^2 \leq 1$ . The spherical limit ( $p = q = 1$ ) is of course the familiar singular isothermal sphere. [If desired, models with a finite core-radius  $R_c$  can be obtained by adding  $R_c^2$  to the term in parentheses in the expression for the potential. These models are recognized as the triaxial generalization of the axisymmetric power-law galaxies (Evans 1993, 1994)].

As will become apparent, there is much advantage in working in conical coordinates  $(r, \mu, \nu)$  defined as follows. The first coordinate  $r$  is the distance to the origin, so that  $r^2 = x^2 + y^2 + z^2$ , where  $(x, y, z)$  are the standard Cartesian coordinates. The variables  $\mu$  and  $\nu$  are angles. They are the solutions for  $\tau$  of

$$\frac{x^2}{\tau - 1} + \frac{y^2}{\tau - p^2} + \frac{z^2}{\tau - q^2} = 0, \quad (2.4)$$

with  $p$  and  $q$  constants that satisfy the condition  $0 \leq q \leq p \leq 1$ . This is a quadratic equation for  $\tau$  with two real roots, which we order so that  $q^2 \leq \nu \leq p^2 \leq \mu \leq 1$ . Some properties of these coordinates, including the relation with the standard spherical coordinates  $(r, \theta, \phi)$ , are given in Appendix A (see also Morse & Feschbach 1953).

Figure 1 illustrates the  $(\mu, \nu)$  coordinate curves on the sphere. The angular coordinates  $\mu$  and  $\nu$  have a center at  $\mu = \nu = p^2$ , which lies at  $\phi = 0$  and  $\theta = \theta_f$ , with

$$\sin^2 \theta_f = T \equiv \frac{1 - p^2}{1 - q^2}, \quad (2.5)$$

where  $T$  is the triaxiality parameter (e.g., Franx, Illingworth & de Zeeuw 1991). While each choice of  $p$  and  $q$  defines a conical coordinate system, all choices which lead to the same

value of  $T$  correspond to the same set of coordinates.

The logarithmic ellipsoidal models are the simplest members of the more general family of *logarithmic scale-free models* which have potentials of the form:

$$\Phi(r, \mu, \nu) = \frac{1}{2} v_c^2 \ln r^2 g(\mu, \nu). \quad (2.6)$$

The function  $g(\mu, \nu)$  is arbitrary, and describes the angular dependence of the potential. We write the density distribution in our models in the general form:

$$\rho(r, \mu, \nu) = \frac{h(\mu, \nu)}{r^\alpha}. \quad (2.7)$$

Here  $h(\mu, \nu)$  is another arbitrary function that describes the angular dependence of the density. When  $\rho$  is the self-consistent density, then  $\alpha = 2$  and the functions  $h(\mu, \nu)$  and  $g(\mu, \nu)$  are related by the Poisson equation  $4\pi G \rho = \nabla^2 \Phi$ . This case is useful for the description of the dominant, dark matter component of haloes. When  $\alpha > 2$ , the density law describes a tracer population (such as Population II stars or globular clusters) that resides in the halo but falls off faster than the dark matter. The Laplacian in conical coordinates is given in equation (A6). We find:

$$h(\mu, \nu) = \frac{1}{(\mu - \nu)g^2} \left\{ (\mu - \nu)g^2 + g \left[ w'(\nu) \frac{\partial g}{\partial \nu} - w'(\mu) \frac{\partial g}{\partial \mu} \right] + 2w(\nu) \left[ g \frac{\partial^2 g}{\partial \nu^2} - \left( \frac{\partial g}{\partial \nu} \right)^2 \right] - 2w(\mu) \left[ g \frac{\partial^2 g}{\partial \mu^2} - \left( \frac{\partial g}{\partial \mu} \right)^2 \right] \right\},$$

where  $w(\tau) = (\tau - 1)(\tau - p^2)(\tau - q^2)$ , and the prime indicates the derivative with respect to the argument. We have taken  $4\pi G = 1$  and  $v_c = 1$ .

The logarithmic ellipsoidal models are just a special case with a simple form of  $g(\mu, \nu)$ :

$$g(\mu, \nu) = \frac{\mu\nu}{p^2 q^2}. \quad (2.8)$$

The associated self-consistent density (2.2) can be written in the form (2.7) with  $\alpha = 2$  and with:

$$h(\mu, \nu) = \frac{1}{\mu^2 \nu^2} [2p^2 q^2 (\mu + \nu) - (p^2 + q^2 + p^2 q^2) \mu \nu]. \quad (2.9)$$

In what follows, we derive Jeans solutions for general scale-free densities in logarithmic scale-free potentials in the next Section, but return to the self-consistent logarithmic ellipsoidal models as our illustrative examples in Sections 4 and 5.

### 3 THE JEANS EQUATIONS

#### 3.1 Conical Coordinates

As Binney & Tremaine (1987) point out, there is a fundamental defect with the Jeans equations – namely, that there is no equation of state relating the components of the velocity dispersion to the density. Any method of solving the Jeans equations therefore requires assumptions regarding either the shape or the orientation of the velocity ellipsoid. And, of course, the usefulness of such solutions depends on whether the assumptions are physically motivated.

We believe that Jeans solutions aligned roughly with conical coordinates do correspond to physical distribution functions for triaxial scale-free models. There are three reasons for this. First, the motion in the separable models

is described naturally in ellipsoidal coordinates, and many positive definite distribution functions exist (Statler 1987; Hunter & de Zeeuw 1992). At large radii the density in separable models becomes scale-free, and the ellipsoidal coordinates reduce to conical coordinates. Hence, the velocity ellipsoid is conically aligned. Second, in the Jeans solutions of axisymmetric scale-free models (see de Zeeuw, Evans & Schwarzschild 1996; Evans, Häfner & de Zeeuw 1997), approximate distribution functions are constructed for solutions close to alignment in spherical polar coordinates. Conical coordinates appear to be the most natural generalisation of this result to triaxial scale-free models. Finally, Amendt & Cuddeford (1991) have argued that Jeans solutions for which the kurtosis vanishes can be regarded as physical. For triaxial scale-free models, the vanishing of the kurtosis implies alignment in conical coordinates. These arguments are suggestive, rather than rigorous, but they seem worth pursuing to us.

Let us consider a triaxial halo with a gravitational potential  $\Phi = \Phi(r, \mu, \nu)$  and with a phase-space distribution function  $f = f(r, \mu, \nu, v_r, v_\mu, v_\nu)$ . In equilibrium,  $f$  must satisfy the collisionless Boltzmann equation (Binney & Tremaine 1987, §4.1) which, in conical coordinates, becomes:

$$0 = r v_r \frac{\partial f}{\partial r} + \left( v_\mu^2 + v_\nu^2 - r \frac{\partial \Phi}{\partial r} \right) \frac{\partial f}{\partial v_r} - v_r v_\mu \frac{\partial f}{\partial v_\mu} - v_r v_\nu \frac{\partial f}{\partial v_\nu} + \frac{1}{Q} \left[ v_\mu \frac{\partial f}{\partial \mu} + \left( \frac{v_\nu^2}{2(\mu - \nu)} - \frac{\partial \Phi}{\partial \mu} \right) \frac{\partial f}{\partial v_\mu} - \frac{v_\mu v_\nu}{2(\mu - \nu)} \frac{\partial f}{\partial v_\nu} \right] + \frac{1}{R} \left[ v_\nu \frac{\partial f}{\partial \nu} + \left( \frac{v_\mu^2}{2(\nu - \mu)} - \frac{\partial \Phi}{\partial \nu} \right) \frac{\partial f}{\partial v_\nu} - \frac{v_\nu v_\mu}{2(\nu - \mu)} \frac{\partial f}{\partial v_\mu} \right],$$

where  $Q$  and  $R$  are the metric coefficients given in equation (A5). Multiplication by  $v_r$ ,  $v_\mu$ , and  $v_\nu$ , respectively, and subsequent integration over velocity space, gives the Jeans equations. These relate the mass density  $\rho$  and the elements of the stress tensor  $\rho \langle v_i v_j \rangle$  (with  $i, j$  equal to  $r, \mu, \nu$ ) to the forces. We obtain

$$\frac{\partial \rho \langle v_r^2 \rangle}{\partial r} + \frac{\rho}{r} [2 \langle v_r^2 \rangle - \langle v_\mu^2 \rangle - \langle v_\nu^2 \rangle] + \frac{1}{rQ} \left[ \frac{\partial \rho \langle v_r v_\mu \rangle}{\partial \mu} + \frac{\rho \langle v_r v_\mu \rangle}{2(\mu - \nu)} \right] + \frac{1}{rR} \left[ \frac{\partial \rho \langle v_r v_\nu \rangle}{\partial \nu} + \frac{\rho \langle v_r v_\nu \rangle}{2(\nu - \mu)} \right] = -\rho \frac{\partial \Phi}{\partial r}, \quad (3.1a)$$

$$\frac{\partial \rho \langle v_r v_\mu \rangle}{\partial r} + 3 \frac{\rho}{r} \langle v_r v_\mu \rangle + \frac{1}{rR} \left[ \frac{\partial \rho \langle v_\mu v_\nu \rangle}{\partial \nu} + \frac{\rho \langle v_\mu v_\nu \rangle}{(\nu - \mu)} \right] + \frac{1}{rQ} \left[ \frac{\partial \rho \langle v_\mu^2 \rangle}{\partial \mu} + \frac{\rho (\langle v_\mu^2 \rangle - \langle v_\nu^2 \rangle)}{2(\mu - \nu)} \right] = -\frac{\rho}{rQ} \frac{\partial \Phi}{\partial \mu}, \quad (3.1b)$$

$$\frac{\partial \rho \langle v_r v_\nu \rangle}{\partial r} + 3 \frac{\rho}{r} \langle v_r v_\nu \rangle + \frac{1}{rQ} \left[ \frac{\partial \rho \langle v_\nu v_\mu \rangle}{\partial \mu} + \frac{\rho \langle v_\nu v_\mu \rangle}{(\mu - \nu)} \right] + \frac{1}{rR} \left[ \frac{\partial \rho \langle v_\nu^2 \rangle}{\partial \nu} + \frac{\rho (\langle v_\nu^2 \rangle - \langle v_\mu^2 \rangle)}{2(\nu - \mu)} \right] = -\frac{\rho}{rR} \frac{\partial \Phi}{\partial \nu}. \quad (3.1c)$$

These three relations between the six stresses  $\rho \langle v_r^2 \rangle$ ,  $\rho \langle v_\mu^2 \rangle$ ,  $\rho \langle v_\nu^2 \rangle$ ,  $\rho \langle v_r v_\mu \rangle$ ,  $\rho \langle v_r v_\nu \rangle$ , and  $\rho \langle v_\mu v_\nu \rangle$  must be satisfied at any point in a triaxial halo model with potential  $\Phi$  and mass density  $\rho$ . A solution of these equations for given  $\rho$  and  $\Phi$  corresponds to a physical equilibrium model only if it is associated with a distribution function  $f(r, \mu, \nu, v_r, v_\mu, v_\nu) \geq 0$ .

These three partial differential equations must be supplied with boundary conditions. The stresses must all vanish

at infinity. Furthermore, the factor  $(\mu - \nu)$  vanishes at the special point  $\mu = \nu = p^2$ . In order to avoid singularities in the terms on the left-hand side, when  $\mu = \nu = p^2$  we must have (c.f., Evans & Lynden-Bell 1989)

$$\langle v_\mu^2 \rangle = \langle v_\nu^2 \rangle, \quad \langle v_\mu v_\nu \rangle = \langle v_r v_\mu \rangle = \langle v_r v_\nu \rangle = 0. \quad (3.2)$$

At this point, the velocity ellipsoid is isotropic in the angular direction. However, the radial dispersion  $\langle v_r^2 \rangle$  may differ from  $\langle v_\mu^2 \rangle = \langle v_\nu^2 \rangle$  here.

### 3.2 The Scale-Free Ansatz

The potential (2.6) and density (2.7) have the desirable attribute of scale-freeness. Their properties at radius  $r' = kr$  follow from those at radius  $r$  by a simple magnification, and by a rescaling of the time variable  $t' = kt$ . For example,  $\rho(kr, \mu, \nu) = k^{-\alpha} \rho(r, \mu, \nu)$ . We consider distribution functions that are also scale-free, i.e., that satisfy  $f(kr, \mu, \nu, v_r, v_\mu, v_\nu) = k^{-\alpha} f(r, \mu, \nu, v_r, v_\mu, v_\nu)$ . The associated stresses then have the following form:

$$\begin{aligned} \rho \langle v_r^2 \rangle &= \frac{F_1(\mu, \nu)}{r^\alpha}, & \rho \langle v_\mu v_\nu \rangle &= \frac{F_4(\mu, \nu)}{r^\alpha}, \\ \rho \langle v_\mu^2 \rangle &= \frac{F_2(\mu, \nu)}{r^\alpha}, & \rho \langle v_r v_\mu \rangle &= \frac{F_5(\mu, \nu)}{r^\alpha}, \\ \rho \langle v_\nu^2 \rangle &= \frac{F_3(\mu, \nu)}{r^\alpha}, & \rho \langle v_r v_\nu \rangle &= \frac{F_6(\mu, \nu)}{r^\alpha}, \end{aligned} \quad (3.3)$$

where  $F_1, F_2, F_3, F_4, F_5$  and  $F_6$  are functions of  $\mu, \nu$ . A necessary - but not sufficient - condition for the stresses (3.3) to correspond to a physical equilibrium model is that  $F_1, F_2, F_3 \geq 0$ , since they give the velocity average of the non-negative quantities  $v_r^2, v_\mu^2$ , and  $v_\nu^2$ .  $F_4, F_5$  and  $F_6$  may be negative, but we always require that the eigenvalues of the stress tensor are non-negative. Even then, not all such solutions correspond to positive distribution functions.

Substitution of the forms (3.3) into the Jeans equations leads to a system of three partial differential equations for the six variables  $F_{1,\dots,6}$ . We find :

$$\begin{aligned} (\alpha - 2)F_1 + F_2 + F_3 &= h + \frac{1}{Q} \left[ \frac{\partial F_5}{\partial \mu} + \frac{F_5}{2(\mu - \nu)} \right] \\ &+ \frac{1}{R} \left[ \frac{\partial F_6}{\partial \nu} + \frac{F_6}{2(\nu - \mu)} \right] \end{aligned} \quad (3.4a)$$

$$\begin{aligned} \left[ \frac{\partial F_2}{\partial \mu} + \frac{F_2 - F_3}{2(\mu - \nu)} \right] &= -\frac{h}{2g} \frac{\partial g}{\partial \mu} + Q(\alpha - 3)F_5 \\ &- \frac{Q}{R} \left[ \frac{\partial F_4}{\partial \nu} + \frac{F_4}{(\nu - \mu)} \right], \end{aligned} \quad (3.4b)$$

$$\begin{aligned} \left[ \frac{\partial F_3}{\partial \nu} + \frac{F_3 - F_2}{2(\nu - \mu)} \right] &= -\frac{h}{2g} \frac{\partial g}{\partial \nu} + R(\alpha - 3)F_6 \\ &- \frac{R}{Q} \left[ \frac{\partial F_4}{\partial \mu} + \frac{F_4}{(\mu - \nu)} \right] \end{aligned} \quad (3.4c)$$

We shall find it convenient to refer to the right-hand sides of (3.4a), (3.4b) and (3.4c) as  $K_1(\mu, \nu), K_2(\mu, \nu)$  and  $K_3(\mu, \nu)$ , respectively. We are free to pick three of the six functions  $F_{1,\dots,6}$  arbitrarily and solve (3.4) for the other three.

### 3.3 Solution for Conical Alignment

Suppose we pick  $F_4, F_5$  and  $F_6$  and solve for  $F_1, F_2$  and  $F_3$ . This choice is motivated by the fact that it is then easy to

consider the special case  $F_{4,5,6} \equiv 0$ , in which the velocity ellipsoid is everywhere aligned exactly along the conical coordinate system. We are particularly interested in this alignment, as we have argued that it is likely to correspond to physical distribution functions.

For the special case  $\alpha = 2$  (the dark halo case), a simple approach can be used. In this case  $F_1$  drops out of equation (3.4a). We use the remaining relation to rewrite (3.4b, c) as follows:

$$\begin{aligned} \frac{\partial F_2}{\partial \mu} + \frac{F_2}{\mu - \nu} &= \frac{h}{2} \left[ \frac{1}{\mu - \nu} - \frac{1}{g} \frac{\partial g}{\partial \mu} \right] + \frac{c_2}{2(\mu - \nu)}, \\ \frac{\partial F_3}{\partial \nu} + \frac{F_3}{\nu - \mu} &= \frac{h}{2} \left[ \frac{1}{\nu - \mu} - \frac{1}{g} \frac{\partial g}{\partial \nu} \right] + \frac{c_3}{2(\mu - \nu)}, \end{aligned} \quad (3.5)$$

where the functions  $c_2(\mu, \nu)$  and  $c_3(\mu, \nu)$  are defined as

$$\begin{aligned} c_2 &= 2 \frac{Q}{R} \left[ F_4 + (\nu - \mu) \frac{\partial F_4}{\partial \nu} \right] + \frac{1}{Q} \left[ \frac{\partial F_5}{\partial \mu} + \frac{F_5}{2(\mu - \nu)} \right] \\ &- 2(\mu - \nu) Q F_5 + \frac{1}{R} \left[ \frac{\partial F_6}{\partial \nu} + \frac{F_6}{2(\nu - \mu)} \right], \end{aligned} \quad (3.6a)$$

$$\begin{aligned} c_3 &= 2 \frac{R}{Q} \left[ F_4 + (\mu - \nu) \frac{\partial F_4}{\partial \mu} \right] + \frac{1}{Q} \left[ \frac{\partial F_5}{\partial \mu} + \frac{F_5}{2(\mu - \nu)} \right] \\ &- 2(\nu - \mu) R F_6 + \frac{1}{R} \left[ \frac{\partial F_6}{\partial \nu} + \frac{F_6}{2(\nu - \mu)} \right]. \end{aligned} \quad (3.6b)$$

Equations (3.5a) and (3.5b) can be integrated separately, by using  $\mu - \nu$  and  $\nu - \mu$ , respectively, as integrating factors. The result is

$$\begin{aligned} F_2 &= \frac{1}{2(\mu - \nu)} \left[ G_2(\mu, \nu) + C_2(\mu, \nu) + D(\nu) \right], \\ F_3 &= \frac{1}{2(\nu - \mu)} \left[ G_3(\mu, \nu) + C_3(\mu, \nu) + \hat{D}(\mu) \right], \end{aligned} \quad (3.7)$$

where, for the moment, the functions  $D(\nu)$  and  $\hat{D}(\mu)$  are arbitrary, and we have introduced the functions

$$\begin{aligned} G_2 &= \int^\mu dm h(m, \nu) \left[ 1 + \frac{(\nu - m)}{g(m, \nu)} \frac{\partial g(m, \nu)}{\partial m} \right], \\ G_3 &= \int^\nu dn h(\mu, n) \left[ 1 + \frac{(\mu - n)}{g(\mu, n)} \frac{\partial g(\mu, n)}{\partial n} \right], \end{aligned} \quad (3.8)$$

and

$$C_2 = \int^\mu dm c_2(m, \nu), \quad C_3 = \int^\nu dn c_3(\mu, n), \quad (3.9)$$

so that  $G_2$  and  $G_3$  depend only on the chosen density and potential. Equation (3.7) gives the general solution for  $F_2$  and  $F_3$  when  $\alpha = 2$ , subject to the requirement on the functions  $\hat{D}(\mu)$  and  $D(\nu)$  imposed by the boundary conditions (3.2), and by equation (3.4a). This latter requirement can be written as:

$$\hat{D}(\mu) - D(\nu) = 2(\mu - \nu)h + G_3 - G_2 + C_3 - C_2. \quad (3.10)$$

The boundary condition (3.2) then shows that  $\hat{D}(p^2) = D(p^2)$ , so that we can in fact consider  $\hat{D}$  and  $D$  the same function  $\Delta(\tau)$ , with  $\Delta(\mu) = \hat{D}(\mu)$  and  $\Delta(\nu) = D(\nu)$ . When  $F_4, F_5$  and  $F_6$  are chosen such that the right-hand side of this equation can be written as a difference  $\Delta(\mu) - \Delta(\nu)$ , then the entire Jeans solution is specified:  $F_1$  is also arbitrary (but non-negative), and  $F_2$  and  $F_3$  are given by (3.7). Otherwise, one can specify only two of the three functions

$F_4$ ,  $F_5$ , and  $F_6$ , and attempt to solve equation (3.10) for the third. For  $F_{4,5,6} \equiv 0$  both  $c_2$  and  $c_3$  vanish, and the solutions without cross terms in the stress tensor have  $C_2 \equiv C_3 \equiv 0$ .

When  $\alpha \neq 2$  (the tracer population case), it is best to differentiate (3.4b) with respect to  $\nu$ , differentiate (3.4c) with respect to  $\mu$  and subtract, to obtain the following equation for the difference  $F^*(\mu, \nu) = F_2(\mu, \nu) - F_3(\mu, \nu)$ :

$$\frac{\partial^2 F^*}{\partial \mu \partial \nu} + \left( \frac{\partial}{\partial \nu} - \frac{\partial}{\partial \mu} \right) \frac{F^*}{2(\mu - \nu)} = \frac{\partial K_2}{\partial \nu} - \frac{\partial K_3}{\partial \mu}. \quad (3.11)$$

The right-hand side of (3.11) contains only known functions. This equation for  $F^*(\mu, \nu)$  is identical to an equation solved by Evans & Lynden-Bell (1989) by the method of Green's functions. If the initial data  $F^*(p^2, \nu)$  and  $F^*(\mu, q^2)$  is provided, then  $F^*(\mu, \nu)$  is given everywhere as a double integral over the Green's function (Evans & Lynden-Bell 1989, section 4). Once we have the difference  $F^*(\mu, \nu)$ , then it is straightforward to solve for the individual components:

$$F_2(\mu, \nu) = F_2(p^2, \nu) + \int_{p^2}^{\mu} dm \frac{F^*(m, \nu)}{2(m - \nu)}. \quad (3.12)$$

With  $F_2(\mu, \nu)$  and  $F_3(\mu, \nu)$  now available,  $F_1(\mu, \nu)$  is obtained by re-arranging (3.4a). Therefore, the boundary conditions required are: (i) the difference  $F^*(\mu, \nu) = F_2(\mu, \nu) - F_3(\mu, \nu)$  on the surface  $\mu = p^2$  and on  $\nu = q^2$ , together with (ii) the value of either  $F_2(\mu, \nu)$  or  $F_3(\mu, \nu)$  on either  $\mu = p^2$  or on  $\nu = q^2$ .

## 4 THE LOGARITHMIC ELLIPSOIDAL HALO

### 4.1 Intrinsic and Projected Shapes

In this section, we return to the logarithmic ellipsoidal models – partly for their astrophysical importance, partly for their simplicity. The density law (2.2) is sensibly positive whenever

$$q^2 + p^2 q^2 - p^2 > 0. \quad (4.1)$$

The physically allowed domain is illustrated as the hatched region in Figure 2. The oblate models have  $p^2 = 1$ , while prolate models have  $p^2 = q^2$ . Although the equipotential surfaces are ellipsoidal, the density figures deviate from a pure ellipsoidal shape. Cross-sections of the intrinsic shape with the three principal planes for the model with  $p = 0.9$  and  $q = 0.8$  are shown in Figure 3. The axis ratios of the density distribution are

$$\begin{aligned} \left( \frac{a_2}{a_1} \right)^2 &= \frac{p^2(p^2 q^2 + p^2 - q^2)}{q^2 + p^2 - p^2 q^2}, \\ \left( \frac{a_3}{a_1} \right)^2 &= \frac{q^2(p^2 q^2 + q^2 - p^2)}{q^2 + p^2 - p^2 q^2}. \end{aligned} \quad (4.2)$$

For our example with  $p = 0.9$  and  $q = 0.8$ , the density contours have semiaxes in the ratio 1 : 0.774 : 0.489. The flattening in the density is of course greater than the flattening in the potential.

In order to calculate the projected shape, we choose new coordinates  $(x'', y'', z'')$  with the  $z''$ -axis along the line of sight, and the  $x''$ -axis in the  $(x, y)$ -plane (see e.g., de Zeeuw & Franx 1989). The  $z$ -axis of the triaxial model projects onto the  $y''$  axis, and  $x''$  and  $y''$  are Cartesian coordinates in the plane of the sky. The various transformations needed

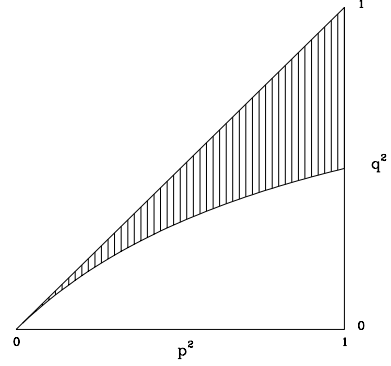


**Figure 2.** The logarithmic ellipsoidal models have density distributions that are everywhere positive in a hatched region of the  $(p^2, q^2)$ -plane. Oblate models have  $p^2 = 1$ , while prolate models have  $p^2 = q^2$ .

to calculate the projected surface density are summarised in Appendix B. The required integration reduces to an integral given in Appendix C of Evans & de Zeeuw (1994). The projected surface density  $\Sigma(x'', y'')$  is analytic for all viewing angles  $(\vartheta, \varphi)$ , namely:

$$\Sigma(x'', y'') = \pi p q \frac{x''^2 + y''^2}{(c_1 x''^2 - c_2 x'' y'' + c_3 y''^2)^{3/2}}. \quad (4.3)$$

where

$$\begin{aligned} c_1 &= \sin^2 \varphi + p^2 \cos^2 \varphi, \\ c_2 &= 2(1 - p^2) \sin \varphi \cos \varphi \cos \vartheta, \\ c_3 &= \cos^2 \varphi \cos^2 \vartheta + p^2 \sin^2 \varphi \cos^2 \vartheta + q^2 \sin^2 \vartheta, \end{aligned} \quad (4.4)$$

When the direction of observation lies in one of the three principal planes ( $\vartheta = \pi/2, \varphi = 0, \varphi = \pi/2$ ), the coefficient  $c_2$  vanishes, and the principal axes of the projected surface density lie along the  $x''$ - and  $y''$ -directions. However, for all other viewing directions  $c_2 \neq 0$  (for triaxial models with  $p \neq 1$ ), the minor axis of the projection is misaligned from the projected short axis of the model, which by definition falls along the  $y''$ -axis. Since our models are scale-free in projection, the misalignment is independent of radius. Figure 4 gives contour plots for the projected surface density of the model with  $p = 0.9, q = 0.8$  for three different viewing directions.

Let us introduce polar coordinates  $(R', \Theta)$  in the sky plane, defined by the relations  $x'' = -R' \sin \Theta, y'' = R' \cos \Theta$ . So, the position angle  $\Theta$  is defined with respect to the  $y''$ -axis and is measured in the counter-clockwise direction. The projected surface density is  $\Sigma \propto S(\Theta)/R'$ . The resulting formula can be simplified further by introducing the two parameters

$$\begin{aligned} \bar{\mu} &= \frac{1}{2}(c_1 + c_3) + \frac{1}{2}\sqrt{(c_3 - c_1)^2 + c_2^2}, \\ \bar{\nu} &= \frac{1}{2}(c_1 + c_3) - \frac{1}{2}\sqrt{(c_3 - c_1)^2 + c_2^2}. \end{aligned}$$

These are the conical coordinates  $(\bar{\mu}, \bar{\nu})$  of the direction of observation defined by the angles  $(\vartheta, \varphi)$  (c.f. eq. [5.4] of de Zeeuw & Franx (1989)). We obtain:

$$\Sigma(R', \Theta) = \frac{2^{3/2} \pi p q}{R' [\bar{\mu} + \bar{\nu} - (\bar{\mu} - \bar{\nu}) \cos(2\Theta - 2\Theta_*)]^{3/2}}, \quad (4.5)$$

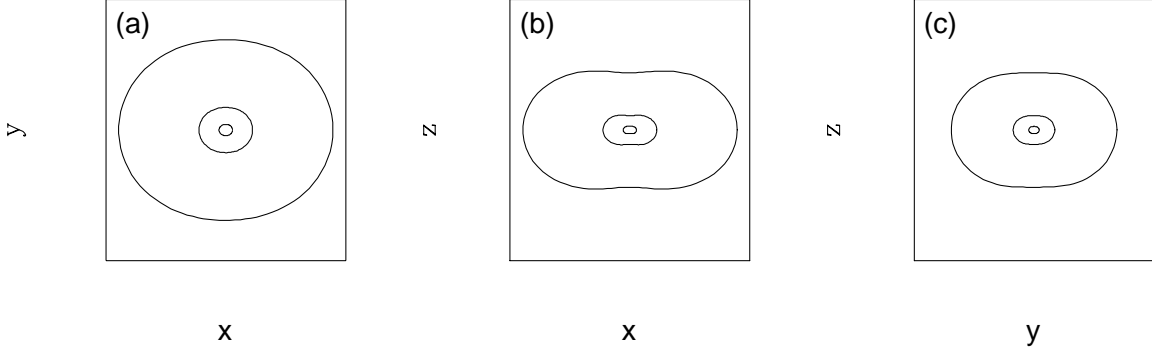


**Figure 3.** Contour plots of the intrinsic density in the principal planes for the logarithmic ellipsoidal model with  $p = 0.9$  and  $q = 0.8$ .

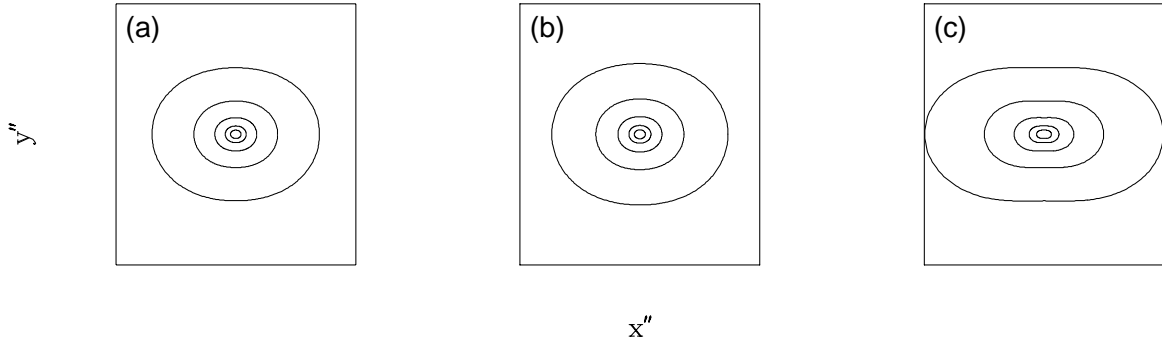


**Figure 4.** Projected surface density for the logarithmic ellipsoidal model with  $p = 0.9$  and  $q = 0.8$ , and three different directions of observation, namely a)  $\vartheta = 0^\circ$  and  $\varphi = 0^\circ$ , b)  $\vartheta = 30^\circ$  and  $\varphi = 45^\circ$ , and c)  $\vartheta = 90^\circ$  and  $\varphi = 90^\circ$ .

where we have defined the misalignment angle  $\Theta_*$  by

$$\tan 2\Theta_* = \frac{c_2}{c_3 - c_1}. \quad (4.6)$$

If  $\Theta_*$  satisfies equation (4.6), then so does  $\Theta_* + \pi/2$ . If we choose  $\Theta_*$  to be the root for which  $(c_3 - c_1) \cos 2\Theta_* + c_2 \sin 2\Theta_* < 0$ , then  $\Theta_*$  is the position angle of the major axis, as measured counter-clockwise from the  $y''$ -axis. Our expression (4.6) for the misalignment angle is identical to that found for the classical ellipsoids, in which the density is stratified on similar concentric ellipsoids with semi-axes  $1 : p : q$  (c.f. Stark 1977). Since the potentials (2.6) are stratified on such ellipsoids, the major axis of the projected potential (and hence the projected surface density) must lie along a position angle  $\Theta_*$ . The axis ratio  $b'/a'$  of the isophotes, defined by the condition  $\Sigma(b', \Theta_* - \frac{\pi}{2}) = \Sigma(a', \Theta_*)$ , is given by

$$\frac{b'}{a'} = \left(\frac{\bar{\nu}}{\bar{\mu}}\right)^{3/2}. \quad (4.7)$$

If  $p = 0.9$  and  $q = 0.8$ , the projected surface density has a shape roughly like E3 if  $\vartheta = \varphi = 0^\circ$  and like E5 if  $\vartheta = \varphi =$

$90^\circ$  (see Figure 4).

## 4.2 Velocity Second Moments

We now carry through the algorithm of Section 3 and find a simple set of velocity dispersions that support the logarithmic ellipsoidal model. Since  $\alpha = 2$ ,  $F_1$  is arbitrary, while  $F_4 = F_5 = F_6$  all vanish for conical alignment. Upon substitution of the expressions for  $g(\mu, \nu)$  and  $h(\mu, \nu)$ , the integrals in (3.7) can be carried out and we obtain:

$$F_2(\mu, \nu) = \frac{1}{2(\mu - \nu)} \left[ (p^2 + q^2 + p^2 q^2 - \frac{2p^2 q^2}{\nu}) \frac{1}{\mu} - \frac{p^2 q^2}{\mu^2} + D(\nu) \right], \quad (4.8a)$$

$$F_3(\mu, \nu) = \frac{1}{2(\nu - \mu)} \left[ (p^2 + q^2 + p^2 q^2 - \frac{2p^2 q^2}{\mu}) \frac{1}{\nu} - \frac{p^2 q^2}{\nu^2} + \hat{D}(\mu) \right]. \quad (4.8b)$$

The condition  $F_2 + F_3 = h$  can be satisfied by the following choice:

$$\Delta(\tau) = \frac{3p^2 q^2}{\tau^2} - \frac{p^2 + q^2 + p^2 q^2}{\tau} + A, \quad (4.9)$$

with  $\Delta$  either the function  $D$  or the function  $\hat{D}$ ,  $\tau$  respectively either  $\nu$  or  $\mu$ , and  $A$  is a constant. The requirement that  $F_2$  and  $F_3$  are finite at the point  $\mu = \nu = p^2$  means that the term in square brackets must vanish there. This means that we must choose  $A = 0$ . The expressions for  $F_2$  and  $F_3$  can then be simplified to

$$\begin{aligned} F_2 &= \frac{1}{2\mu^2\nu^2} [(3\mu + \nu)p^2 q^2 - (p^2 + q^2 + p^2 q^2)\mu\nu], \\ F_3 &= \frac{1}{2\mu^2\nu^2} [(\mu + 3\nu)p^2 q^2 - (p^2 + q^2 + p^2 q^2)\mu\nu]. \end{aligned} \quad (4.10)$$

Despite the symmetry of  $F_2$  and  $F_3$  with respect to  $\mu$  and  $\nu$ , the velocity ellipsoid is anisotropic everywhere, except at the point  $\mu = \nu = p^2$ . Here  $F_2 = F_3$ , while  $F_1$  remains arbitrary.

To gain insight into a physically reasonable choice for  $F_1$ , let us consider the spherical limit ( $p = q = 1$ ). The logarithmic ellipsoidal model becomes the well-known singular isothermal sphere. The angular stresses corresponding to (4.10) become

$$\langle v_\mu^2 \rangle = \langle v_\nu^2 \rangle = \frac{1}{2}, \quad (4.11)$$

This is recognised as the Jeans solution generated by the constant anisotropy distribution functions for the isothermal sphere (see eq. [5.10] in Evans (1994)). The full solutions for the spherically aligned stresses are

$$\langle v_r^2 \rangle = \frac{1}{2 + \gamma}, \quad \langle v_\theta^2 \rangle = \langle v_\phi^2 \rangle = \frac{1}{2}, \quad (4.12)$$

where  $\gamma$  is a constant anisotropy parameter. In the spherical limit,  $\gamma = 0$  gives an isotropic solution,  $\gamma \rightarrow -2$  is the radial orbit model, while  $\gamma \rightarrow \infty$  is the circular orbit model. This suggests a possible choice for  $F_1$  as

$$F_1 = \frac{g(\mu, \nu)}{2 + \gamma} = \frac{\mu\nu}{(2 + \gamma)p^2 q^2}. \quad (4.13)$$

Any choice for  $F_1$  satisfies the Jeans equations. This choice (4.13) has the advantage that the spherical limit ( $p^2 = q^2 = 1$ ) certainly corresponds to a positive definite distribution function for any choice of anisotropy parameter  $\gamma > -2$ . The inclusion of the term  $g(\mu, \nu)$  in (4.13) additionally ensures that the axisymmetric limit ( $p^2 = 1$ ) with  $\gamma = 0$  has the same stresses as the two integral distribution function (see eq. (2.3) of Evans (1993)). It is clearly heartening that the checkable limits do correspond to physical models. Even so, the triaxial models probably only have physical distribution functions for some range in  $\gamma$  near to the isotropic value. Strongly anisotropic models are known to be afflicted by instabilities, like the radial orbit instability (e.g., Palmer 1994). Henceforth, we only consider models in which the inequality in any two semi-axes of the velocity dispersion tensor is no greater than 3 : 1.

Given our solutions for  $F_1$ ,  $F_2$  and  $F_3$ , the intrinsic velocity second moments of the logarithmic ellipsoidal model

are found through (3.3) as;

$$\begin{aligned} \langle v_r^2 \rangle &= \frac{\mu^3 \nu^3}{(2 + \gamma)p^2 q^2 [2(\mu + \nu)p^2 q^2 - (p^2 + q^2 + p^2 q^2)\mu\nu]}, \\ \langle v_\mu^2 \rangle &= \frac{1}{2} \frac{(3\mu + \nu)p^2 q^2 - (p^2 + q^2 + p^2 q^2)\mu\nu}{2(\mu + \nu)p^2 q^2 - (p^2 + q^2 + p^2 q^2)\mu\nu}, \\ \langle v_\nu^2 \rangle &= \frac{1}{2} \frac{(\mu + 3\nu)p^2 q^2 - (p^2 + q^2 + p^2 q^2)\mu\nu}{2(\mu + \nu)p^2 q^2 - (p^2 + q^2 + p^2 q^2)\mu\nu}. \end{aligned} \quad (4.14)$$

The relationship between conicals  $(\mu, \nu)$  and familiar Cartesian coordinates is given in eqs. (A1) and (A2). This furnishes an analytic and realistic set of stresses that support the logarithmic ellipsoidal model – a prototype for a triaxial dark matter halo. This is one of the main results of the paper.

The logarithmic ellipsoidal model, much like the isothermal sphere itself, does not obey the virial theorem (e.g., Binney & Tremaine 1987, Gerhard 1991). In fact, the velocity dispersions (4.14) have a curious property – the total kinetic energy is not fixed, and the radial velocity dispersion may be changed independently of the angular velocity dispersions. The same property holds for the isothermal sphere itself, as is evident from (4.12). It is a surprising feature, as we expect increases in the radial velocity dispersion to be balanced by decreases in the angular dispersions. In fact, both isothermal spheres and ellipsoids make complete sense when regarded as the inner parts of finite mass models. For example, the truncated, flat rotation curve model (Wilkinson & Evans 1999) has a density that varies like  $r^{-2}$  within a scalelength  $a$  so that:

$$\rho(r) = \frac{a^3}{r^2(r^2 + a^2)^{3/2}}, \quad \Phi(r) = -\log\left[\frac{\sqrt{r^2 + a^2} + a}{r}\right], \quad (4.15)$$

where, as for the logarithmic ellipsoidal model, we are using units with  $v_c = 4\pi G = 1$ . The radial velocity dispersion is (see eq. (11) of Wilkinson & Evans (1999))

$$\begin{aligned} \langle v_r^2 \rangle &= \left(\frac{r}{a}\right)^{\gamma+2} \frac{(r^2 + a^2)^{3/2}}{a^3} \int_0^\Phi \frac{\sinh^{5+\gamma} \phi}{\cosh^3 \phi} d\phi, \\ \langle v_\phi^2 \rangle &= \left(\frac{r}{a}\right)^{\gamma+2} \frac{(2 + \gamma)(r^2 + a^2)^{3/2}}{2a^3} \int_0^\Phi \frac{\sinh^{5+\gamma} \phi}{\cosh^3 \phi} d\phi. \end{aligned} \quad (4.16)$$

In the inner parts, the rotation curve is flat with unit amplitude and the model looks like the isothermal sphere. In the limit  $r \ll a$ , the crucial point is that the velocity dispersions (4.16) do indeed reduce to those of the isothermal sphere (4.12), as a careful Taylor expansion demonstrates. This is the case for all  $\gamma \geq -2$ . The kinetic energy of the inner, isothermal parts of these models can be increased – as it can be balanced by a loss in the kinetic energy of the outer parts.

## 5 PARTICLE DARK MATTER DETECTION RATES

### 5.1 Preliminaries

The dark matter in galaxy haloes may be composed of weakly-interacting massive particles (WIMPs), which couple to ordinary matter only through electroweak-scale interactions. Particle physics has provided an extensive list of candidates (e.g., Kolb & Turner 1989), of which the lightest

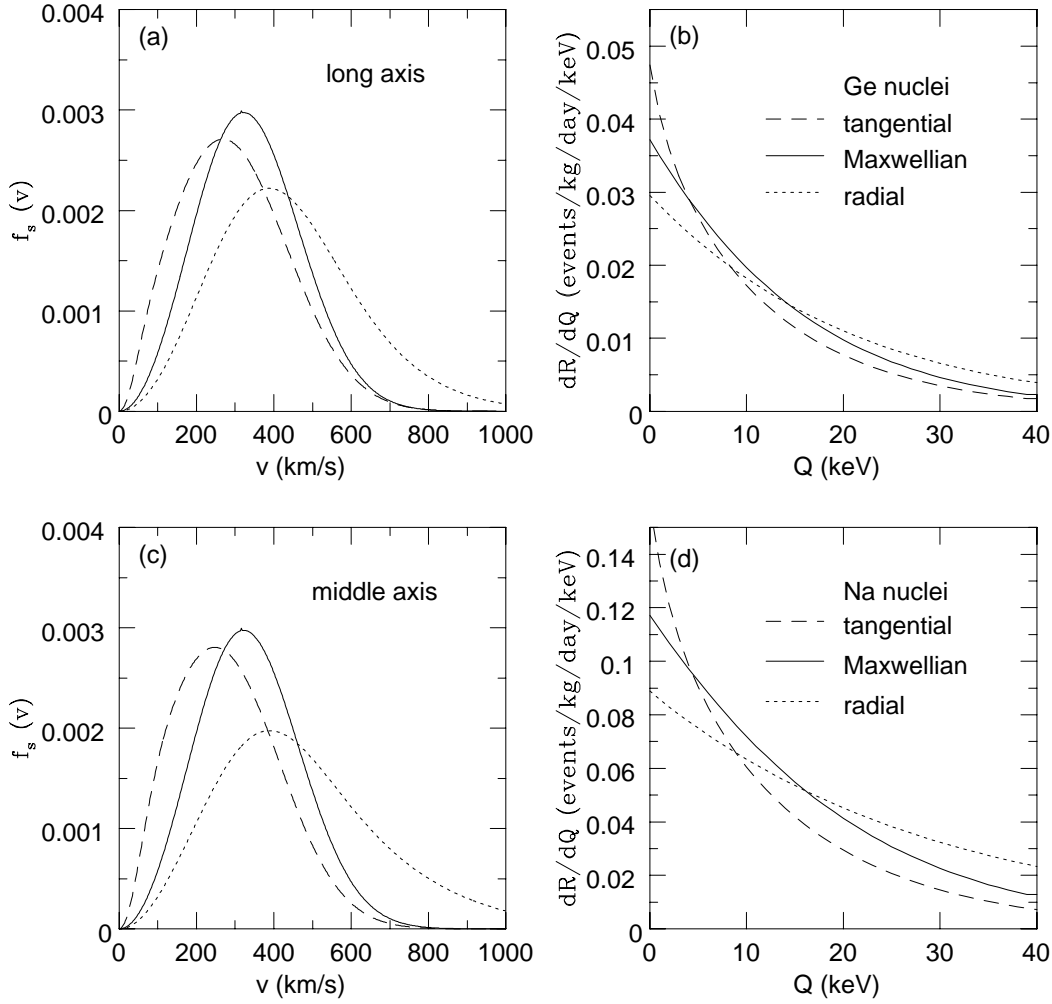


**Figure 5.** The distribution of speeds and the differential rate on the major axis (a,b) and the intermediate axis (c,d) of the logarithmic ellipsoidal model with  $p = 0.9$  and  $q = 0.8$ . In each panel, results are given for a radially anisotropic [ $\gamma = -1.78$ ] solution (dotted line) and tangentially anisotropic [ $\gamma = 16$ ] solution (dashed line), as well as a comparison Maxwellian (full line). Panel (b) assumes that the WIMPs are scattering off  $^{73}\text{Ge}$  nuclei, while panel (d) assumes that they are scattering off  $^{23}\text{Na}$  nuclei. The computations are carried out for the date of June 2nd when the total rate is at a peak.

stable neutral supersymmetric particle (generally the neutralino) is one of the current favourites (e.g., Jungman et al. 1996). One promising way of confirming this hypothesis involves direct detection experiments. Broadly speaking, the experiments work by measuring the recoil energy of a nucleus in a low background laboratory detector which has undergone a collision with a WIMP. The aim is to measure the number of events per day per kilogram of detector material as a function of the recoil energy  $Q$ . Although this deposited energy is minute and the WIMP-nucleus interaction is very rare, there are a number of such experiments in progress around the world. These include the UKDMC collaboration operating in Boulby mine (e.g., Smith et al. 1996), the DAMA collaboration in the Gran Sasso Laboratory (e.g., Bernabei et al. 1999), which both use NaI scintillators, and the CDMS experiment located underground at Stanford University, which uses cryogenic germanium and

silicon detectors (e.g., Gaitskell et al. 1997).

In all these experiments, the detection rate depends on the mass  $m_\chi$  and cross-section  $\sigma_0$  of the WIMP, as well as the mass of the target nucleus  $m_N$  in the detector. But, it also depends on the local dark matter density  $\rho_0$  and the speed distribution  $f_s(v)$  of WIMPs in the Galactic halo near the Earth. Calculations have already been performed using Maxwellian velocity distributions for singular and cored isothermal spheres, as well as for self-consistent flattened halo models (e.g., Freese et al. 1985; Jungman et al. 1996; Kamionkowski & Kinkhabwala 1998; Belli et al. 1999). One of our aims here is to assess the likely uncertainties in the detection rates caused by halo triaxiality and velocity anisotropy. The formulae for the calculation of rates in direct detection experiments are summarised in the review of Jungman et al. (1996). We give here only the bare details.



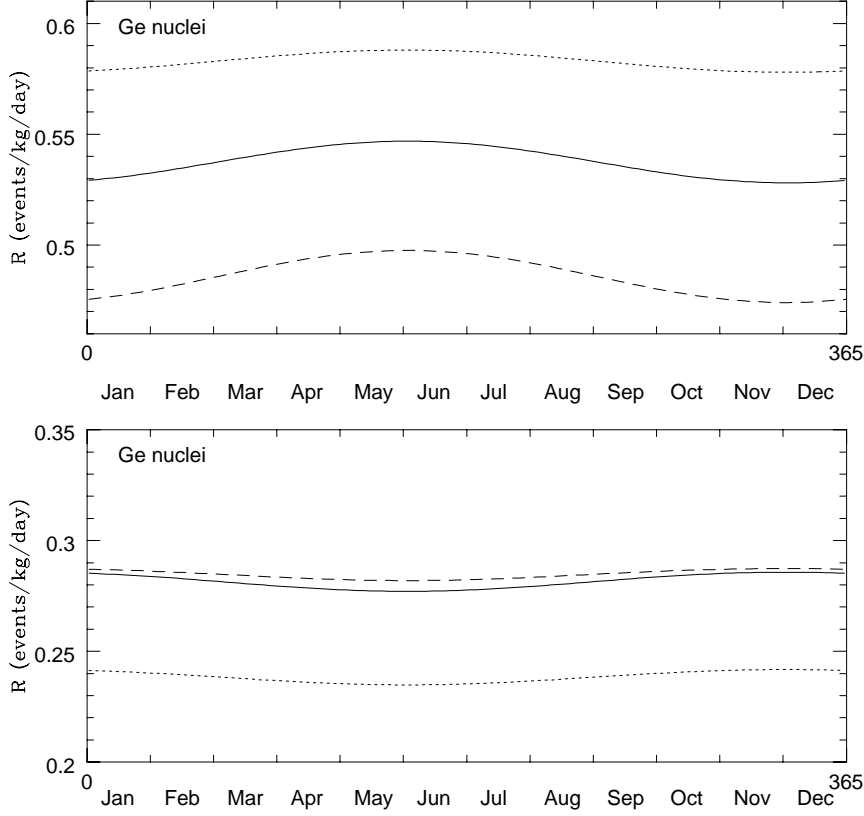


**Figure 6.** The WIMP annual modulation signal is shown for a radially anisotropic [ $\gamma = -1.78$ ] model (dotted line), a tangentially anisotropic [ $\gamma = 16$ ] model (dashed line) and a comparison Maxwellian (full line). The upper panel gives the variation in the total rate, the lower panel the variation in the rate of low energy events ( $< 10$  keV). This calculation assumes 40 GeV WIMPs interacting with  $^{73}\text{Ge}$  nuclei. The halo model has  $p = 0.9$  and  $q = 0.8$ , while the sun is located on the major axis.

The differential rate for WIMP detection is

$$\frac{dR}{dQ} = \frac{\sigma_0 \rho_0}{2m_\chi m_r^2} F^2(Q) \int_{v_{\min}}^{\infty} \frac{f_s(v)}{v} dv, \quad (4.17)$$

where  $R$  is the rate,  $Q$  is the recoil energy and  $m_r = m_N m_\chi / (m_N + m_\chi)$  is the reduced mass,  $F(Q)$  is the nuclear form factor,  $f_s(v)$  is the probability distribution of WIMP speeds relative to the detector, and

$$v_{\min} = \left[ \frac{Q m_N}{2m_r^2} \right]^{1/2}. \quad (4.18)$$

The most commonly-used nuclear form factor is (e.g., Ahlen et al. 1987; Freese et al. 1988; Jungman et al. 1996)

$$F(Q) = \exp\left(-\frac{Q}{2Q_0}\right), \quad (4.19)$$

where  $Q_0$  is the nuclear coherence energy

$$Q_0 = \frac{3\hbar^2}{2m_N R_N^2}, \quad (4.20)$$

and  $R_N$  is the radius of the target nucleus (in cm)

$$R_N = 10^{-13} [0.3 + 0.91(m_N/\text{GeV})^{1/3}]. \quad (4.21)$$

The total event rate can be found by integrating over all detectable energies

$$R = \int_{E_T}^{\infty} \frac{dR}{dQ} dQ, \quad (4.22)$$

where  $E_T$  is the threshold energy for the detector.

As our benchmark model, we take a WIMP with only scalar interactions of mass  $m_\chi = 40$  GeV and a cross-section  $\sigma_0 = 4 \times 10^{-36} \text{ cm}^2$ . We consider two kinds of detectors. The first is a cryogenic detector made of germanium so that  $m_N = 68$  GeV. The second is a scintillation detector made of NaI, for which results are presented for WIMPs scattering off sodium nuclei ( $m_N = 22$  GeV). Threshold effects are neglected, so that  $E_T = 0$ . The local halo density  $\rho_0$  is taken as  $0.3 \text{ GeV cm}^{-3}$ . These values are suggested by Jungman et al. (1996) as a standard set. We note that they are, of course, subject to very substantial uncertainties. In particular, speculations as to WIMP masses range from 10 GeV to a few TeV. WIMPs may have both scalar and spin-dependent interactions with the nucleus. In fact, direct detection experiments are best suited for scalar-coupled WIMPs, whilst indirect methods (such as searching for WIMP annihilation products, like neutrinos, in the Sun) are more powerful for

spin-coupled WIMPs (Kamionkowski, Griest, Jungman & Sadoulet 1995). Finally, the uncertainty in the local halo density is at least a factor of two, and possibly more (e.g., Bahcall, Schmidt & Soneira 1983; Turner 1986; Gates, Gyuk & Turner 1995)

## 5.2 Triaxiality and Anisotropy

Let us consider two possible locations for the Sun, namely on the long axis ( $x$ -axis) and the intermediate axis ( $y$ -axis) of the triaxial halo. At these locations, the conical coordinates are locally equivalent to cylindrical polar coordinates. So, the velocity distribution in the Earth's rest frame can be approximated as the triaxial Gaussian

$$f = \frac{1}{(2\pi)^{\frac{3}{2}}\sigma_R\sigma_\phi\sigma_z} \exp\left[-\frac{v_R^2}{2\sigma_R^2} - \frac{(v_\phi + v_\oplus)^2}{2\sigma_\phi^2} - \frac{v_z^2}{2\sigma_z^2}\right]. \quad (4.23)$$

Here, we assume that the Earth moves with respect to the rest frame of the Galaxy with a velocity

$$v_\oplus = 220 \left[ 1.05 + 0.07 \cos\left(\frac{t - t_p}{\text{yr}}\right) \right] \text{ kms}^{-1}, \quad (4.24)$$

where  $t_p$  corresponds to June 2nd. This gives an annual modulation to the WIMP signal, which is of course invaluable in distinguishing it from background events caused by radioactivity and cosmic rays (Freese et al. 1988). Even though many of the experiments operate underground to cut down the effects from cosmic rays and use high-purity material to minimise the effects of radioactivity, it is still true that the background rate is a few events per kilogram per day. This is larger than that rate expected from WIMP interactions by a factor of  $\sim 10$ . The WIMP signal is expected to attain a maximum in early June and a minimum in early December. Recently, the DAMA group has claimed detection of this modulation (Bernabei et al. 1999a,b), although their interpretation has been contested by others (Gerber et al. 1999; Abusaiadi et al. 2000).

On the major axis, the Jeans solution (4.14) becomes

$$\begin{aligned} \sigma_R^2 = \langle v_R^2 \rangle &= \frac{v_c^2}{(2 + \gamma)(p^{-2} + q^{-2} - 1)}, \\ \sigma_\phi^2 = \langle v_\mu^2 \rangle &= \frac{v_c^2(2q^{-2} - 1)}{2(p^{-2} + q^{-2} - 1)}, \\ \sigma_z^2 = \langle v_\nu^2 \rangle &= \frac{v_c^2(2p^{-2} - 1)}{2(p^{-2} + q^{-2} - 1)}. \end{aligned} \quad (4.25)$$

On the intermediate axis, we have

$$\begin{aligned} \sigma_R^2 = \langle v_R^2 \rangle &= \frac{v_c^2 p^{-4}}{(2 + \gamma)(1 + q^{-2} - p^{-2})}, \\ \sigma_\phi^2 = \langle v_\mu^2 \rangle &= \frac{v_c^2(2q^{-2} - p^{-2})}{2(1 + q^{-2} - p^{-2})}, \\ \sigma_z^2 = \langle v_\nu^2 \rangle &= \frac{v_c^2(2 - p^{-2})}{2(1 + q^{-2} - p^{-2})}. \end{aligned} \quad (4.26)$$

The distribution of WIMP speeds  $f_s(v)$  follows from (4.23) as

$$f_s(v) = \frac{v^2}{(2\pi)^{\frac{3}{2}}\sigma_R\sigma_\phi\sigma_z} \int_0^\pi d\alpha \sin\alpha \int_0^{2\pi} d\beta \exp\left[-\frac{(v \cos\alpha + v_\oplus)^2}{2\sigma_\phi^2} - \frac{v^2 \sin^2\alpha \sin^2\beta}{2\sigma_R^2} - \frac{v \sin^2\alpha \cos^2\beta}{2\sigma_z^2}\right].$$

It is now straightforward to calculate the differential rate (4.17) for any of our triaxial, anisotropic halo models.

Figure 5 shows the distribution of speeds and the differential rate for the logarithmic ellipsoidal halo with  $p = 0.9$  and  $q = 0.8$ . The Sun is located on the major axis ( $x$ -axis) for panels (a) and (b), the intermediate axis ( $y$ -axis) for panels (c) and (d). The curves are drawn for a radially anisotropic and a tangentially anisotropic velocity distribution that supports the triaxial figure. Also shown is the standard curve obtained by assuming a spherical halo with a Maxwellian velocity distribution (c.f., Fig. 22 of Jungman et al. 1996). Panel (b) shows the case when the WIMPs interact with germanium detector nuclei, while panel (d) the case of sodium nuclei. The effects of triaxiality and velocity anisotropy can cause the total rate to vary by  $\sim 20\%$  in the case of germanium and by  $\sim 40\%$  in the case of sodium. The total rate is greatest for the radial anisotropic velocity distributions, least for the tangential anisotropic. In the case displayed in Figure 5, the radially anisotropic model [ $\gamma = -1.78$ ] has a broader distribution of speeds. This gives larger incident WIMP velocities, and so more events at higher energies. The converse is true for the tangentially anisotropic model [ $\gamma = 16$ ], which generate more events at lower energies.

More important than the differential rate is the size of the annual modulation effect. The upper panel of Figure 6 shows the variation in the total rate during the course of the year for the radially and tangentially anisotropic halo models. This is for the case of 40 GeV WIMPs impinging on germanium nuclei. Also shown is the comparison Maxwellian of the isothermal sphere, for which the annual modulation effect is already small; the peak to peak variation over the course of the year is just  $\sim 0.019$  events/kg/day. For the radially anisotropic model, this halves to  $\sim 0.010$  events/kg/day, while for the tangentially anisotropic model, this increases slightly to  $\sim 0.024$  events/kg/day. Let us recall that the modulation must be detected against a background rate that is at least a factor of 10 greater than the underlying WIMP event rate. Even if the WIMP velocities are described by a Maxwellian, the detection of the annual modulation is hard enough. It is disconcerting to find that the modulation amplitude can halve on moving to radially anisotropic, flattened models. The lower panel of Figure 6 shows the variation in the rate of low energy events only ( $< 10$  keV). The amplitude of the modulation is severely attenuated. For all the velocity distributions, the peak to peak variation is very low, at most 0.008 events/kg/day. Indeed, even the sign of the modulation has reversed, and the maximum number of events now occurs in December, not June (c.f., Hasenbalg 1998).

The DAMA group (Bernabei et al., 1999a,b) have recently extracted statistical evidence for the annual modulation signal in the low energy events using nine 9.7 kg NaI detectors. It is therefore interesting to carry out the calculations for this case as well. Figure 7 shows the annual variation in rate for WIMPs scattering off sodium nuclei in NaI detectors. Again, we see that the annual modulation in the total rate is weakest in the radially anisotropic model, showing a peak to peak variation of 0.08 events/kg/day; for the tangentially anisotropic model, it is 0.12 events/kg/day. The lower panel shows the modulation in the rate of events with *measured* energies less than 10 keV. Nuclear recoils of energies in the 1-20 keV range produce little ionisation as they

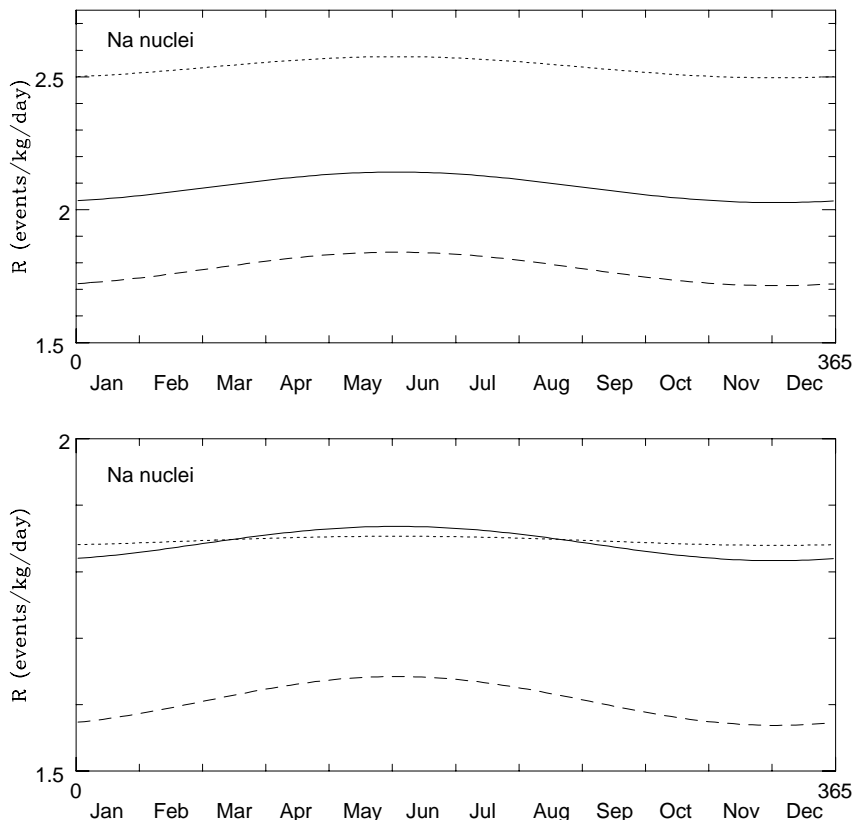


**Figure 7.** As Figure 6, but the calculation assumes 40 GeV WIMPs scattering off  $^{23}\text{Na}$  nuclei. The upper panel shows the variation in total rate, the lower panel the variation in the rate of low energy events ( $< 10$  keV) assuming a quenching factor of 0.3.

lose energy; most of the energy goes into phonons. Hence, ionisation or scintillation detectors are much less efficient than cryogenic detectors. Accordingly, we have included a “quenching factor” of 0.3 to account for the efficiency of the detector (Spooner et al. 1994; Bernabei et al. 1996); a measured energy of 10 keV corresponds to a nuclear recoil energy of  $\sim 33$  keV. We see that the peak to peak variation in the low energy events (which is where DAMA have claimed evidence of the signal) is sensitive to the anisotropy. The lowest variation is just 0.01 events/kg/day for the radially anisotropic model; this rises to 0.07 events/kg/day for the tangentially anisotropic model. Reversed modulation (i.e., the maximum occurring in December) still occurs, but the quenching drives it to still lower energy ranges. For example, it occurs for events with measured energies less than 5 keV in the models with both Maxwellian and radially anisotropic velocity distributions.

## 6 CONCLUSIONS

In this paper, we have presented a paradigm for the triaxial dark halo. The logarithmic ellipsoidal model is the natural generalisation of the isothermal sphere into the triaxial domain. Many of its properties are disarmingly simple – including the potential, mass density and projected surface density. This paper has provided simple, analytic solutions

of the Jeans equations for the logarithmic ellipsoidal model, under the assumption of conical alignment of the velocity ellipsoid. These solutions give the components of the velocity dispersion tensor required to hold up the triaxial halo against gravity. In this paper, we have adopted the approximation that the velocity distribution is a triaxial Gaussian with semiaxes equal to the velocity dispersions as specified by our solutions of the Jeans equations. While this distribution function does not satisfy Jeans theorem (e.g., Binney & Tremaine 1987), it does have the right stresses or momentum flux to hold the halo up against gravity. The logarithmic ellipsoidal models therefore provide simple prototypes for the density and velocity distributions of triaxial haloes.

Solutions of the Jeans equations contain as a subset the models which have physical meaning, i.e., which have a non-negative distribution function. Building distribution functions in the triaxial case is not easy, since only the energy is known to be an exact integral of motion in the general case. Merritt & Fridman (1996), following up an earlier suggestion by Schwarzschild (1993), have provided numerical evidence that cusped triaxial systems may undergo slow evolution towards axisymmetry. This may mean that exact distribution functions for such models do not exist – leaving the Jeans equations as one of the few possible investigative tools for these slowly evolving systems.

As an application, we have considered direct detection

rates of particle dark matter. Weakly-interacting massive particle (WIMP) detection experiments typically measure the nuclear recoil energy as the WIMPs collide with detector nuclei. Predictions for WIMP detection rates are habitually carried out using the isothermal sphere to model the dark matter distribution. This paper has provided calculations for more realistic triaxial dark haloes with anisotropic velocity distributions. Standard isothermal sphere calculations give estimates for the total rate that are good to within  $\sim 20\%$  for Ge detectors and to within  $\sim 40\%$  for NaI detectors. Both the shape of the differential rate distribution and the size of the annual modulation effect are sensitive to the velocity distributions. In pessimistic cases, the modulation amplitude roughly halves on moving to radially anisotropic and flattened models, rendering detection of this characteristic WIMP signature even harder. In optimistic cases, tangentially anisotropic models can give slightly higher peak to peak changes than standard isothermal spheres, although the total rate is smaller. Assuming a WIMP mass of 40 GeV and a cross-section  $\sigma_0 = 4 \times 10^{-36} \text{ cm}^2$  for Ge nuclei, then the peak to peak variation in the total rate over the year may then be as low as  $\sim 0.010$  events/kg/day or as high as  $\sim 0.024$  events/kg/day, with the maximum occurring in June and the minimum in December.

If only the low energy events are considered, then the amplitude of the modulation is smaller still and even the sign of the correlation can reverse. The greatest number of low energy events can occur in December, not June. The energy at which this crossover happens depends on the anisotropy and triaxiality of the halo, as well as the detector material. In practice, direct detection experiments monitor the number of events within energy intervals chosen by the experimenter. It would be interesting to calculate the optimum energy ranges for detection of both the modulation in the high energy events and the reversed modulation in the low energy events. In such difficult experiments, where the background is typically ten times or more as strong as the signal, this effect should be exploited to provide a convincing and unambiguous signature of actual detection.

## ACKNOWLEDGMENTS

It is a pleasure to record our gratitude to the late Martin Schwarzschild for many stimulating conversations. NWE acknowledges financial support from the Royal Society. He thanks Subir Sarkar for many invaluable discussions on particle dark matter and Gilles Gerbier for pointing out the importance of quenching. CMC and PTdZ thank the Institute for Advanced Study, Princeton, and the sub-Department of Theoretical Physics, Oxford, for hospitality.

## REFERENCES

- Abusaidi R., et al. 2000, *Phys. Rev. Lett.*, in press  
 Ahlen S.P., Avignone F.T., Brodzinski R.L., Drukier A.K., Gelmini G., Spergel D.N., 1987, *Phys. Lett. B*, 195, 603  
 Amendt P., Cuddeford P., 1991, *ApJ*, 368, 79  
 Bacon R., 1985, *A&A*, 143, 84  
 Bahcall J.N., Schmidt M., Soneira M., 1983, *ApJ*, 265, 730  
 Barnes J., in "Formation and Evolution of Galaxies", eds., C. Munoz-Tunon, F. Sanchez, (Cambridge University Press, Cambridge), p. 233  
 Bernabei R. et al., 1996, *Phys. Lett. B*, 389, 757  
 Bernabei R. et al., 1999a, *Phys. Lett. B*, 424, 195  
 Bernabei R. et al., 1999b, *Phys. Lett. B*, 450, 448  
 Belli P. et al., 1999, *Phys. Rev.*, D61, 023512  
 Binney J.J., 1981, *MNRAS*, 196, 455  
 Binney J.J., Mamon G.A., 1982, *MNRAS*, 200, 361  
 Binney J., Tremaine S., 1987, *Galactic Dynamics*, (Princeton University Press, Princeton)  
 de Zeeuw P.T., Evans N.W., Schwarzschild M., 1996, *MNRAS*, 280, 903  
 de Zeeuw P.T., Franx M., 1989, *ApJ*, 343, 617  
 de Zeeuw P.T., Pfenniger D., 1988, *MNRAS*, 235, 949 Erratum: 262, 1088.  
 Evans N.W., 1993, *MNRAS*, 260, 191  
 Evans N.W., 1994, *MNRAS*, 267, 333  
 Evans N.W., de Zeeuw P.T., 1994, *MNRAS*, 271, 202  
 Evans N.W., Häfner R.M., de Zeeuw P.T., 1997, *MNRAS*, 286, 315  
 Evans N.W., Lynden-Bell D., 1989, *MNRAS*, 236, 801  
 Fillmore, J.A., 1986, *AJ*, 91, 1096  
 Franx M., 1988, *MNRAS*, 231, 285  
 Franx M., Illingworth G.D., de Zeeuw P.T., 1991, *ApJ*, 383, 112  
 Freese K., Frieman J., Gould A., 1988, *Phys. Rev.*, D37, 3388  
 Gaitskell R.J. et al., 1997, in "The Identification of Dark Matter", ed. N.J.C. Spooner, (World Scientific, Singapore), p. 440.  
 Gates E.I., Gyuk G., Turner M.S., 1995, *ApJ*, L123, 449  
 Gerbier G., Mallet J., Mosca L., Tao C., 1997, *astro-ph/9710181*  
 Gerbier G., Mallet J., Mosca L., Tao C., 1999, *astro-ph/9902194*  
 Gerhard O.E., 1991, *MNRAS*, 250, 812  
 Häfner R.M., Evans N.W., Dehnen W., Binney J.J., 2000, *MNRAS*, 314, 433  
 Hasenbalg F., 1998, *Astropart. Phys.*, 9, 339  
 Hunter C., de Zeeuw P.T., 1992, *ApJ*, 389, 79  
 Jungman G., Kamionkowski M., Griest K., 1996, *Phys. Rep.*, 267, 195  
 Kamionkowski M., Griest K., Jungman G., Sadoulet B., 1995, *Phys. Rev. Lett.*, 74, 5174  
 Kamionkowski M., Kinkhabwala A., 1998, *Phys. Rev.*, D57, 3256  
 Klapdor-Kleingrothaus H.V., Ramachers Y., 1997, *Dark Matter in Astro and Particle Physics*, (Kluwer, Dordrecht)  
 Kolb E.W., Turner M.S., 1989, *The Early Universe*, (Addison-Wesley, Redwood City)  
 Lewin J.D., Smith P.F., 1996, *Astropart. Phys.*, 4, 387  
 Merritt D., Fridman T., 1996, *ApJ*, 460, 136  
 Miralda-Escudé J., Schwarzschild M., 1989, *ApJ*, 339, 752  
 Morse P.M., Feshbach H., 1953, *Methods of Theoretical Physics* (McGraw-Hill, 1953)  
 Olling R.P., 1995, *AJ*, 110, 591  
 Olling R.P., 1996, *AJ*, 112, 457  
 Paczyński B., 1986, *ApJ*, 304, 1  
 Palmer P.L., 1994, *Stability of Collisionless Stellar Systems*, (Kluwer, Dordrecht)  
 Richstone D.O., 1980, *ApJ*, 238, 103  
 Sackett P., Rix H.-W., Jarvis B.J., Freeman K.C., 1994, *ApJ*, 436, 629  
 Schwarzschild M., 1979, *ApJ*, 232, 236  
 Schwarzschild M., 1981, in "The Structure and Evolution of Normal Galaxies", eds. S.M. Fall, D. Lynden-Bell, (Cambridge University Press, Cambridge), p. 43  
 Schwarzschild M., 1982, *ApJ*, 263, 599  
 Schwarzschild M., 1993, *ApJ*, 409, 563  
 Smith P.F. et al., 1996, *Phys. Lett. B*, 379, 299  
 Spooner N.J.C., 1997, *The Identification of Dark Matter*, (World Scientific, Singapore)  
 Spooner N.J.C. et al., 1994, *Phys. Lett. B*, 321, 156  
 Stark A.A., 1977, *ApJ*, 213, 368  
 Statler T.S., 1987, *ApJ*, 321, 113  
 Toomre A., 1982, *ApJ*, 259, 535

Turner M.S., 1986, Phys. Rev., D33, 889  
 Wilkinson M.I., Evans N.W., 1999, MNRAS, 310, 645  
 Zhao H.S., 1996, MNRAS, 283, 149

## APPENDIX A: CONICAL COORDINATES

Here, we collect some properties of the conical coordinates  $(r, \mu, \nu)$  defined in Section 2.1. The two roots  $\mu$  and  $\nu$  of equation (2.4) are

$$\mu, \nu = \frac{1}{2}(k_1 \pm \sqrt{k_2}), \quad (\text{A1})$$

with

$$\begin{aligned} r^2 k_1 &= (y^2 + z^2) + p^2(x^2 + z^2) + q^2(x^2 + y^2), \\ r^4 k_2 &= [(p^2 - q^2)x^2 + (1 - q^2)y^2 + (1 - p^2)z^2]^2 \\ &\quad + 4(1 - p^2)(1 - q^2)y^2 z^2. \end{aligned} \quad (\text{A2})$$

It follows that  $\mu + \nu = k_1$  and  $4\mu\nu = k_1^2 - k_2$  are each simple rational functions of  $x^2$ ,  $y^2$ , and  $z^2$ . The inverse transformations are:

$$\begin{aligned} x^2 &= \frac{r^2(1 - \mu)(1 - \nu)}{(1 - p^2)(1 - q^2)}, & y^2 &= \frac{r^2(\mu - p^2)(p^2 - \nu)}{(1 - p^2)(p^2 - q^2)}, \\ z^2 &= \frac{r^2(\mu - q^2)(\nu - q^2)}{(1 - q^2)(p^2 - q^2)}, \end{aligned} \quad (\text{A3})$$

so that each point  $(r, \mu, \nu)$  corresponds to eight points  $(\pm x, \pm y, \pm z)$ . The standard spherical coordinates  $(r, \theta, \phi)$  are related to the conical coordinates by

$$\begin{aligned} \cos^2 \theta &= \frac{(\mu - q^2)(\nu - q^2)}{(1 - q^2)(p^2 - q^2)}, \\ \tan^2 \phi &= \frac{(\mu - p^2)(p^2 - \nu)(1 - q^2)}{(1 - \mu)(1 - \nu)(p^2 - q^2)}. \end{aligned} \quad (\text{A4})$$

The metric of the conical coordinate system is given by  $ds^2 = dx^2 + dy^2 + dz^2 = dr^2 + r^2(Q^2 d\mu^2 + R^2 d\nu^2)$ , with

$$Q^2 = \frac{\nu - \mu}{4w(\mu)}, \quad R^2 = \frac{\mu - \nu}{4w(\nu)}, \quad (\text{A5})$$

$$w(\tau) = (\tau - 1)(\tau - p^2)(\tau - q^2).$$

The element of area  $dA$  on the sphere of radius  $r$  and the Laplacian  $\nabla^2$  are given by:

$$\begin{aligned} dA &= r^2 Q R d\mu d\nu = \frac{r^2(\mu - \nu)d\mu d\nu}{4\sqrt{-w(\mu)}\sqrt{w(\nu)}}, \\ \nabla^2 &= \frac{1}{r^2} \frac{\partial}{\partial r} r^2 \frac{\partial}{\partial r} + \frac{1}{r^2 Q R} \frac{\partial}{\partial \mu} R \frac{\partial}{\partial \mu} + \frac{1}{r^2 Q R} \frac{\partial}{\partial \nu} R \frac{\partial}{\partial \nu}. \end{aligned} \quad (\text{A6})$$

The relations between the conical and cartesian velocity components can be written as:

$$\begin{aligned} v_x &= \frac{x}{r} \left[ v_r + \frac{v_\mu}{2Q(\mu - 1)} + \frac{v_\nu}{2R(\nu - 1)} \right], \\ v_y &= \frac{y}{r} \left[ v_r + \frac{v_\mu}{2Q(\mu - p^2)} + \frac{v_\nu}{2R(\nu - p^2)} \right], \\ v_z &= \frac{z}{r} \left[ v_r + \frac{v_\mu}{2Q(\mu - q^2)} + \frac{v_\nu}{2R(\nu - q^2)} \right], \end{aligned} \quad (\text{A7})$$

or, inverting the relations, by:

$$\begin{aligned} v_r &= \frac{xv_x + yv_y + zv_z}{r}, \\ v_\mu &= \frac{2Q}{(\nu - \mu)r} [(\mu - p^2)(\mu - q^2)xv_x \\ &\quad + (\mu - 1)(\mu - q^2)yv_y + (\mu - 1)(\mu - p^2)zv_z], \\ v_\nu &= \frac{2R}{(\mu - \nu)r} [(\nu - p^2)(\nu - q^2)xv_x \\ &\quad + (\nu - 1)(\nu - q^2)yv_y + (\nu - 1)(\nu - p^2)zv_z]. \end{aligned} \quad (\text{A8})$$

## APPENDIX B: THE PROJECTED MOMENTS OF TRIAXIAL MODELS

Here, we derive expressions for the projected moments of a triaxial model. The projected zeroth moment is the surface density, calculated in the main body of the paper. Formulae for the projected first and second velocity moments are also given.

We choose new coordinates  $(x'', y'', z'')$  with the  $z''$ -axis along the line of sight, and the  $x''$ -axis in the  $(x, y)$ -plane (e.g., de Zeeuw & Franx 1989). This means that the  $z$ -axis projects onto the  $y''$ -axis. We define the direction of observation by the viewing angles  $(\vartheta, \varphi)$ , and write  $\mathbf{r} = (x, y, z)$ . Then the coordinate transformation is

$$\mathbf{r}'' = \mathbf{R}_3 \mathbf{r}, \quad \mathbf{r} = \mathbf{R}_3^{-1} \mathbf{r}'', \quad (\text{B1})$$

where

$$\mathbf{R}_3 = \begin{pmatrix} -\sin \varphi & \cos \varphi & 0 \\ -\cos \varphi \cos \vartheta & -\sin \varphi \cos \vartheta & \sin \vartheta \\ \cos \varphi \sin \vartheta & \sin \varphi \sin \vartheta & \cos \theta \end{pmatrix}, \quad (\text{B2})$$

$$\mathbf{R}_3^{-1} = \begin{pmatrix} -\sin \varphi & -\cos \varphi \cos \vartheta & \cos \varphi \sin \vartheta \\ \cos \varphi & -\sin \varphi \cos \vartheta & \sin \varphi \sin \vartheta \\ 0 & \sin \vartheta & \cos \theta \end{pmatrix}.$$

The projected surface density is  $\Sigma$  where:

$$\Sigma(x'', y'') = \int dz'' \rho(\mathbf{R}_3^{-1} \mathbf{r}''). \quad (\text{B3})$$

The major and minor axis of the projected surface density  $\Sigma$  of a triaxial galaxy generally do not line up with the  $x''$ - and  $y''$ -axes, but lie at a position angle  $\Theta_* \neq 0$ . The expression for  $\Theta_*$  is given in eq. (4.6). Let  $(x', y')$  be Cartesian coordinates on the plane of the sky aligned with the principal axes of the projected density. Then;

$$\mathbf{r}'' = \mathbf{R}_2 \mathbf{r}', \quad \mathbf{r}' = \mathbf{R}_2^{-1} \mathbf{r}'', \quad (\text{B4})$$

where

$$\mathbf{R}_2 = \begin{pmatrix} \cos \Theta_* & -\sin \Theta_* & 0 \\ \sin \Theta_* & \cos \Theta_* & 0 \\ 0 & 0 & 1 \end{pmatrix}, \quad (\text{B5})$$

$$\mathbf{R}_2^{-1} = \begin{pmatrix} \cos \Theta_* & \sin \Theta_* & 0 \\ -\sin \Theta_* & \cos \Theta_* & 0 \\ 0 & 0 & 1 \end{pmatrix}.$$

For completeness, let us also outline the calculation of the projected velocity moments. By differentiation with respect to time, we find for the velocity components:

$$\dot{\mathbf{r}}'' = \mathbf{R}_3 \dot{\mathbf{r}}, \quad \dot{\mathbf{r}} = \mathbf{R}_3^{-1} \dot{\mathbf{r}}''. \quad (\text{B6})$$

At a fixed position, we can calculate the intrinsic mean motion by integrating over all velocities weighted by the normalised velocity distribution function. Subsequent integration along the line of sight, weighted with the density distribution, then gives the observed mean motions:

$$\langle \mu_{x''} \rangle = \frac{1}{\Sigma} \int_{-\infty}^{\infty} dz'' \rho \langle \dot{x}'' \rangle, \quad \langle \mu_{y''} \rangle = \frac{1}{\Sigma} \int_{-\infty}^{\infty} dz'' \rho \langle \dot{y}'' \rangle, \quad (\text{B7})$$

$$\langle v_{\text{los}} \rangle = \langle \mu_{z''} \rangle = \frac{1}{\Sigma} \int_{-\infty}^{\infty} dz'' \rho \langle \dot{z}'' \rangle,$$

The projected second moments follow in a similar way; for example, the diagonal components of the second-rank tensor are

$$\langle \mu_{x''x''}^2 \rangle = \frac{1}{\Sigma} \int_{-\infty}^{\infty} dz'' \rho \langle \dot{x}''^2 \rangle, \quad \langle \mu_{y''y''}^2 \rangle = \frac{1}{\Sigma} \int_{-\infty}^{\infty} dz'' \rho \langle \dot{y}''^2 \rangle, \quad (\text{B8})$$

$$\langle v_{\text{los}}^2 \rangle = \langle \mu_{z''z''}^2 \rangle = \frac{1}{\Sigma} \int_{-\infty}^{\infty} dz'' \rho \langle \dot{z}''^2 \rangle.$$

and similarly for the mixed components. The products of the velocity components in the integrand can be found by use of equation (B6).

This paper has been produced using the Royal Astronomical Society/Blackwell Science  $\text{\TeX}$  macros.